Yun *et al. Biochar* (2022) 4:66
https://doi.org/10.1007/s42773-022-00189-4

Biochar

ORIGINAL RESEARCH Open Access

Pb(II) adsorption by biochar from co-pyrolysis of corn stalks and alkali-fused fly ash

Xiaotong Yun[1†], Yan Ma[1*†], Hao Zheng[2], Yaru Zhang[1], Biying Cui[1] and Baoshan Xing[3]

Abstract

Numerous studies have reported the potential of silica as a biochar (BC) modifier. However, despite its high silica content, fly ash is rarely used for BC modification. Herein, modified BCs were produced by co-pyrolysis of corn stalks with alkali-fused fly ash (AFFA) at 200 and 600 °C (denoted as AFFA/BC). The Pb(II) adsorption mechanism and adsorption performance were investigated. The AFFA/BC had larger specific surface areas than the pure BC samples (2.54–137 vs. 0.50 $m^2\ g^{-1}$) owing to their stable carbon structure. The Pb(II) adsorption capacity of AFFA/BC in water was approximately 6% higher than that of BC owing to the increased cation (Na^+) exchange and new bonding sites, such as C–O and Si–O. AFFA/BC exhibited good Pb(II) adsorption performance in high-concentration simulated wastewater (pH 4–6), with a maximum adsorption capacity of 110.29 mg g^{-1}. The Pb(II) adsorption mechanism was in accordance with the pseudo-second-order kinetic and Langmuir isotherm models. At 25 °C and pH 5, the theoretical Pb(II) adsorption capacities of $AFFA_{200}$/BC and $AFFA_{600}$/BC were 201.66 and 186.81 mg g^{-1}, respectively, compared to 145.98 mg g^{-1} of BC. Physical adsorption, precipitation, cation exchange, and complexation were identified as the main Pb(II) adsorption mechanisms through X-ray photoelectron spectrometry.

Highlights

- A new type of biochar was prepared by co-pyrolysis of corn stalks and alkali-fused fly ash for Pb(II) removal from wastewater.
- The high surface area and Pb(II) adsorption capacity of adsorbents made them suitable for wastewater treatment.
- The main Pb(II) adsorption mechanisms were physisorption, precipitation, cation exchange, and complexation.

Keywords: Biochar, Co-pyrolysis, Alkali-fused fly ash, Lead ion adsorption

†Xiaotong Yun and Yan Ma contributed equally to this work.

*Correspondence: mayan2202@163.com

[1] School of Chemical and Environmental Engineering, China University of Mining and Technology, Beijing 100083, China
Full list of author information is available at the end of the article

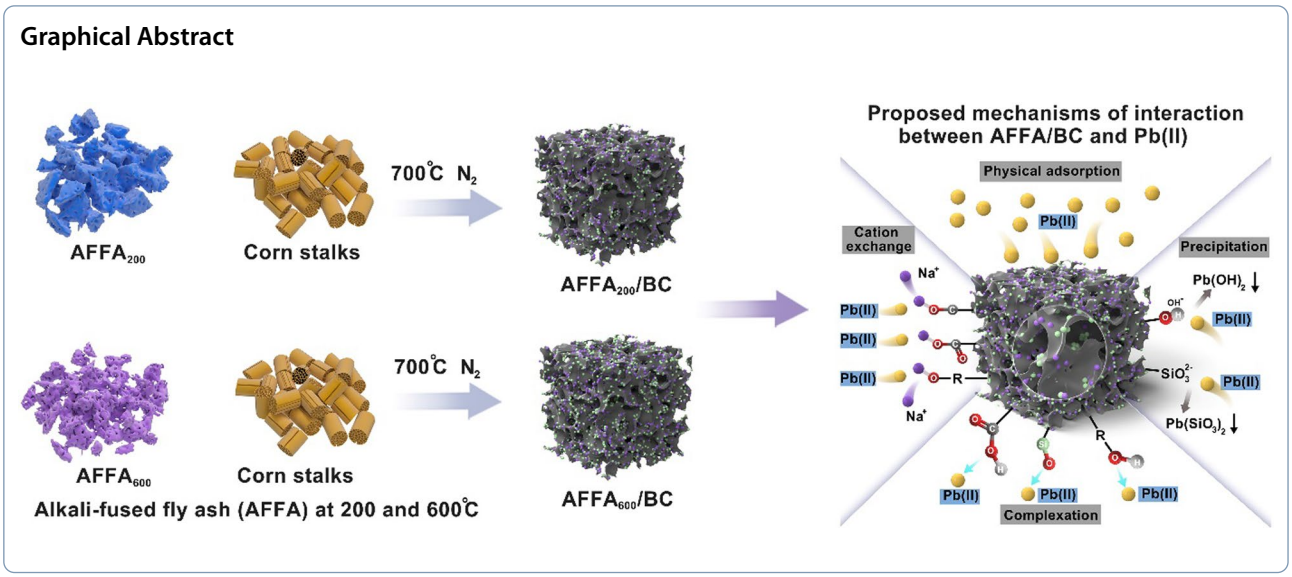

1 Introduction

Pb is a highly toxic metal, and its extensive use has caused widespread environmental pollution and health problems. Pb and its compounds are extremely toxic to humans and other organisms and have long half-lives. Long-term Pb exposure can cause nervous system disorders, cognitive deficits, and affective disorders (Mason et al. 2014). Water is one of the most significant pathways by which heavy metals enter the human body. While some Pb exist naturally in aqueous environments owing to the dissolution of Pb-bearing minerals, most is introduced from the wastewater of Pb mining and smelting processes (Gautam et al. 2016; Masindi and Muedi 2018). Many traditional and technologically advanced methods have been applied to treat wastewater, including ion exchange, chemical precipitation, membrane separation, reverse osmosis, and electrochemical treatment (Cinperi et al. 2019; Gautam et al. 2016; Sarode et al. 2019). Although these methods can treat Pb-containing wastewater to meet discharge standards, they exhibit disadvantages such as incomplete treatment, expensive equipment, high labor and monitoring costs, chemically intensive systems, secondary pollutant generation (e.g., sludge and solid waste), and the need for further treatment (Wadhawan et al. 2020). Therefore, there is a critical need to develop efficient and environmentally friendly adsorbents to remove Pb from wastewaters and other aqueous environments.

Biochar (BC) is a multifunctional material with hydrophilic and acid–base properties owing to its high porosity, large specific surface area, highly stable aromatized structure, and abundant surface functional groups, including hydroxyl or phenolic hydroxyl groups (–OH), carboxyl groups (–COOH), ester groups (–COOR), and aliphatic double bonds (C=C) (Lu et al. 2020). It is usually obtained by pyrolysis of biomass in a low oxygen atmosphere. Notably, BC can remove heavy metals and organic pollutants from water and has broad application prospects for environmental pollution treatment and remediation (Chang et al. 2020; Fang et al. 2020; Nan et al. 2021; Xiong et al. 2017). The most effective methods of improving the adsorption capacity of BC for heavy metals in wastewater are surface modification with functional groups (e.g., $–NH_2$, –COOH, –SH) and coating with oxides and other substances (Liu et al. 2015; Yang et al. 2019).

Silica has attracted much attention as a new BC modifier. By co-pyrolyzing biomass with silica, the resultant BC has a significantly larger number of mesopores, which enhances the pore filling effect of pollutants and is conducive to the adsorption of pollutants from wastewater (Zhao et al. 2019). Furthermore, silicon participates in the formation of carbon structure by forming C–Si bonds, which enhances the stability of BC (Ahmad et al. 2019; Zama et al. 2018; Zhao et al. 2019). Fly ash (FA) is a promising BC modifier owing to its high silica content. Wang et al. (2020) reported that silica-composited BC prepared by co-pyrolysis of biomass (swine manure or rice straw) with alkali-fused fly ash (AFFA) exhibited enhanced methylene blue adsorption performance. Notably, it had a larger specific surface area, more oxygenic functional groups, and more exchangeable Na ions than a comparable BC sample formed without AFFA (Huang et al. 2020a, b; Wang et al. 2020). There are a few reports on the synthesis and heavy metal adsorption capabilities of

BC produced via co-pyrolysis of biomass and AFFA (denoted as AFFA/BC). However, the reactions that occur between AFFA and biomass during co-pyrolysis, as well as its effect on the properties of the BC, remain unclear. Therefore, the adsorption performance of AFFA/BC for aqueous heavy metal ions, influencing factors, and related mechanisms should be further investigated.

In this study, low-cost waste materials, including corn stalk (CS) biomass and FA, were used to prepare a new type of BC. After alkali fusion pretreatment using NaOH to form AFFA, CS and AFFA were uniformly mixed and co-pyrolyzed to obtain new BCs–AFFA/BC. The structural characteristics and chemical compositions of the AFFA and AFFA/BC samples were analyzed by N_2 sorption analysis, scanning electron microscopy (SEM), energy-dispersive X-ray spectroscopy (EDS), X-ray diffraction (XRD), X-ray photoelectron spectroscopy (XPS), and Fourier-transform infrared spectroscopy (FTIR). The Pb(II) adsorption capacity and removal efficiency of the AFFA/BC samples under different influencing factors were also investigated, and AFFA/BCs with high adsorption capacities for heavy metal Pb were screened. Finally, the adsorption mechanisms of the AFFA/BCs were explored through various characterization methods.

2 Materials and methods

2.1 Materials

Analytical grade NaOH, HCl, HNO_3, and $Pb(NO_3)_2$ were purchased from Beijing Chemical Industrial Group Co., Ltd., China. $Pb(NO_3)_2$ standard solution was purchased from the National Research Center for Standard Substances of China. FA was collected from a coal-fired power plant in Shanxi Province, China. FA samples were dried in an oven at 80 °C, passed through an 18-mesh sieve, and stored at ~ 25 °C in airtight bags. Residual CS was obtained from a corn crop field surrounding a coal mining site in Changzhi City, Shanxi Province, China.

2.2 Alkali fusion pretreatment of FA

The FA was pretreated by an alkali fusion process to form AFFA. First, 10 g of oven-dried FA and 15 g of NaOH were evenly mixed in a nickel crucible and heat treated at 200 or 600 °C for 2 h in a muffle furnace. The cooled mixtures were ground to a powder with an agate mortar and passed through an 18-mesh sieve to obtain $AFFA_{200}$ and $AFFA_{600}$, respectively. Part of the $AFFA_{200}$ and $AFFA_{600}$ samples were washed with dilute nitric acid (NA) using a suction filter until the pH of the filtrate was neutral (Zhao et al. 2020a), followed by drying, grinding, and passing through a 35-mesh sieve to obtain $AFFA_{200}$-NA and $AFFA_{600}$-NA, respectively. Another part of the $AFFA_{200}$ and $AFFA_{600}$ samples were washed with deionized water (DW), dried, and ground to yield $AFFA_{200}$-DW and $AFFA_{600}$-DW, respectively.

2.3 Preparation of AFFA/BC

The AFFA/BC samples were prepared as follows. First, CS was crushed, ground, and passed through an 18-mesh sieve. The six AFFA samples were then mixed with the pretreated CS and DW (AFFA:CS:DW = 1:10:100 w/w/v), and the mixtures were stirred evenly using a magnetic stirrer for 2 h. After drying, grinding, and passing through an 18-mesh sieve, the mixtures were placed in a nickel boat (38 × 19 × 100 mm) and pyrolyzed in a tube furnace in an N_2 atmosphere by heating at 5 °C min^{-1} to 700 °C and holding for 2 h (Wang et al. 2020; Xiao et al. 2018; Yang et al. 2018). The samples were then cooled in the N_2 atmosphere and passed through a 100-mesh sieve to produce the AFFA/BC samples with an average particle size of ~ 0.15 mm. Control samples of pure BC were also prepared under the same pyrolysis conditions but without AFFA.

2.4 Characterization

The Brunauer–Emmett–Teller (BET) specific surface area (S_{BET}), total pore volume (V_{total}), and average pore diameter (D_{avg}) of the samples were analyzed by N_2 sorption analysis using a Micromeritics ASAP-2460 surface area and porosity analyzer (Micromeritics Instrument Corp., USA). The surface morphology and elemental distribution were analyzed by SEM (ZEISS Gemini 300, Germany) with EDS (Smartedx, Germany). XRD (Rigaku RU-200b, Japan) and thermogravimetric analysis (TGA; SDT Q600, Germany) were performed on the AFFA samples to determine the mineral composition and thermal stability, respectively. The C, H, and N contents of the BC and AFFA/BC samples were determined using an automatic elemental analyzer (Vario EL cube, Germany), and the O contents were calculated using Additional file 1: Eq. S1. FTIR (Thermo Scientific Nicolet iS5, Japan) and XPS (Thermo Scientific K-Alpha, Japan) were performed to identify the surface functional groups, atomic structures, and chemical bonds. Pb, As, Cd, and polycyclic aromatic hydrocarbons (PAHs), which might affect the adsorption of Pb(II) by AFFA/BC, were not detected in FA (Additional file 1: Table S1).

2.5 Adsorption experiments

Adsorption experiments were conducted with different initial solution pH (3, 4, 5, and 6), adsorbent dosages (0.8, 1.0, 1.6, 2.0, and 2.4 g L^{-1}), and initial Pb(II) concentrations (5, 10, 20, 50, and 100 mg L^{-1}). The Pb(II)

solutions were prepared by diluting a $Pb(NO_3)_2$ stock solution (1000 mg L^{-1}) with DW. The initial pH of the solution was adjusted to the desired value using 0.1 M NA or NaOH. Adsorption experiments were conducted by mixing the adsorbent (BC or AFFA/BC) with 50 mL of the Pb(II) solution in a 100 mL polyethylene centrifuge tube. The tubes were placed in a thermostatic oscillator at 25 °C and shaken at 160 rpm for 24 h. The supernatant was separated using a 0.45 mm membrane filter, and its metal content was analyzed by inductively coupled plasma-atomic emission spectrometry (ICP-AES, Optima 7000DV). The sorption kinetics were investigated by continuously shaking mixtures of the adsorbent and 20 mg L^{-1} Pb(II) solution at 25 °C for various lengths of time (5–1440 min). The Pb(II) adsorption isotherms were calculated from the results. All experiments were performed in triplicate.

The Pb(II) removal efficiency (w, %) and adsorption capacity (q_e, mg L^{-1}) were calculated using Eqs. 1 and 2, respectively.

$$w = \frac{C_0 - C_e}{C_0} \times 100, \tag{1}$$

$$q_e = \frac{(C_0 - C_t) \times V}{m}, \tag{2}$$

where C_0 and C_t (mg L^{-1}) are the initial Pb(II) concentration and that at time t, respectively, V (L) is the volume of solution, and m (g) is the mass of adsorbent.

The pseudo-first-order (PFO), pseudo-second-order (PSO), and intraparticle diffusion (IPD) models (Additional file 1: Equations S2—S4) were employed to investigate the adsorption mechanisms of Pb(II) on AFFA/BC. The Langmuir and Freundlich models (Additional file 1: Equations S5 and S6) were used to investigate the adsorption characteristics.

3 Results and discussion

3.1 Characterization of AFFA and AFFA/BC

3.1.1 AFFA

SEM images and EDS spectra of the FA, $AFFA_{200}$, and $AFFA_{600}$ samples are shown in Fig. 1. The FA particles were spherical with different sizes and smooth surfaces (Fig. 1a), which was attributed to the aluminosilicate glass phase of FA (Agarwal and Rani 2017; Huang et al. 2020a). The EDS results showed that the FA contained O, Si, Al, Ca, and Mg. Following pretreatment by NaOH, the glass phase structure of FA was destroyed; thus, the $AFFA_{200}$ and $AFFA_{600}$ particles exhibited irregular and rough structures. The surface pores of $AFFA_{600}$ were larger and more numerous than those of $AFFA_{200}$, demonstrating that high-temperature (600 °C) treatment destroyed the original FA structure to a greater extent than low-temperature (200 °C) treatment. Moreover, the EDS results revealed that $AFFA_{200}$ and $AFFA_{600}$ were mainly composed of O, Na, Si, and Al, possibly because the mixed calcination of FA and NaOH introduced O and Na (Agarwal and Rani 2017; Zhao et al. 2020b). Furthermore, compared with FA, the peaks corresponding to Ca and Mg almost disappeared, while the intensity of the O peak increased significantly (Fig. 1b, c). This indicates the successful coverage of O and Na onto the surface of the $AFFA_{200}$

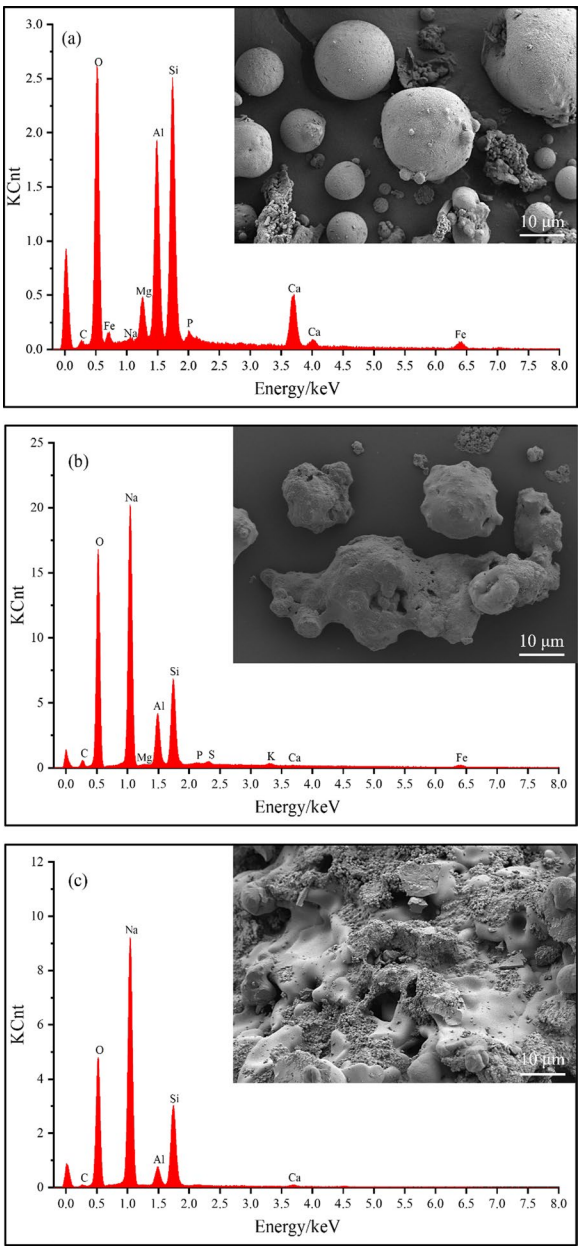

Fig. 1 Scanning electron microscopy and energy-dispersive X-ray spectroscopy characterization of **a** FA, **b** $AFFA_{200}$, and **c** $AFFA_{600}$

and $AFFA_{600}$ particles. Therefore, FA did not undergo crystallization during the alkali fusion pretreatment. In addition, as shown in Additional file 1: Fig. S1, the clear difference in aperture distribution between the $AFFA_{200}$ and $AFFA_{600}$ samples indicates that the AFFA structure was greatly affected by the alkali fusion temperature.

The N_2 adsorption–desorption isotherms of FA, $AFFA_{200}$, and $AFFA_{600}$ are shown in Additional file 1: Fig. S2a. At low relative pressures (P/P_0), all the adsorption–desorption curves were similar. FA had a more uniform pore size and more ordered pores than the other samples, along with the presence of meso- (2–50 nm) (Additional file 1: Fig. S1). However, the adsorption of N_2 by $AFFA_{200}$ and $AFFA_{600}$ was poor, corresponding to significantly smaller S_{BET} values (0.94 and 0.46 $m^2\ g^{-1}$, respectively) compared to that of FA (4.99 $m^2\ g^{-1}$) (Additional file 1: Table S2). This was attributed to the alkali modification treatment, which could have blocked pores or promoted their collapse (Wang et al. 2020). Based on the International Union of Pure and Applied Chemistry (IUPAC) classification (Sing 1985), both open Type I and air-impermeable Type II pores were present in FA. In contrast, $AFFA_{200}$ and $AFFA_{600}$ contained a significantly lower number of Type I pores. Thus, it is likely that the products of alkali fusion (e.g., Na_2O) blocked the pores of the raw material, resulting in more air-impermeable pores in the AFFA samples, as was shown by Huang et al. (2020a).

The inorganic crystal structure database was used for peak matching of the XRD patterns, and the identified peaks of the minerals present in FA, $AFFA_{200}$, and $AFFA_{600}$ are shown in Additional file 1: Figs. S2b–d. The mineral compositions of $AFFA_{200}$ and $AFFA_{600}$ were significantly different from those of FA. FA mainly comprised mullite ($3Al_2O_3{\cdot}2SiO_2$), which is an aluminosilicate mineral, and gypsum ($CaSO_4$). $AFFA_{200}$ contained nepheline ($KNa_3(AlSiO_4)_4$), andalusite (Al_2SiO_5), and jadeite ($NaAl(Si_2O_6)$), which all belong to aluminosilicate mineral. Thus, SiO_2, Al_2O_3, and other stable substances on the FA surface were activated to yield amorphous Si–O and Al–O bonds in $AFFA_{200}$ (Bhagath Singh and Subramaniam 2016). In contrast, the main material components of $AFFA_{600}$ were kyanite ($Al_2(SiO_4)O$) and nepheline (Additional file 1: Fig. S2c). Therefore, parts of the glass structure of FA were destroyed and novel compounds were formed during alkali fusion pretreatment at 200 and 600 °C (Ameh et al. 2016; Zhao et al. 2020b).

TGA was used to investigate the thermal stability of the samples and to determine an appropriate pyrolysis temperature (Additional file 1: Fig. S2e, f). The mass loss of the samples was divided into two stages. The first stage involved the removal of water, corresponding to mass losses of 3.29%, 6.94%, and 0.43% for FA (25–861 °C), $AFFA_{200}$ (25–199 °C), and $AFFA_{600}$ (25–782 °C), respectively. The second stage was characterized by the decomposition of Si–O and Al–O bonds or the loss of residual NaOH (Zhao et al. 2020b), with mass losses of 1.94%, 4.48%, and 6.04% for FA (860.98–980 °C), $AFFA_{200}$ (199–980 °C), and $AFFA_{600}$ (782–980 °C), respectively. Notably, the onset temperature of the second decomposition stage of $AFFA_{200}$ (199 °C) was significantly lower than that of $AFFA_{600}$ (782 °C) and FA (861 °C) (Additional file 1: Fig. S2e). Furthermore, $AFFA_{200}$ exhibited a clear mass loss at approximately 350 °C. These differences were related to the NaOH content of the samples; the alkali fusion temperature of $AFFA_{200}$ (200 °C) was below the melting point of NaOH (318 °C), whereas that of $AFFA_{600}$ (600 °C) was above it. Therefore, $AFFA_{200}$ contained more NaOH than $AFFA_{600}$, resulting in a lower onset temperature of the second decomposition stage. Because $AFFA_{600}$ still contained some NaOH, its second decomposition stage began at a slightly lower temperature than that of FA.

3.1.2 AFFA/BC

The characteristics of the BC and AFFA/BC samples are listed in Table 1. The yields of all the AFFA/BC samples (30.7–34.6%) were higher than that of pure BC (29.1%) owing to the introduction of Na and O from AFFA during co-pyrolysis. Moreover, the yields of $AFFA_{200}$-NA/

Table 1 Basic characteristics of BC and AFFA/BC

Adsorbents	Yield (%)	Ash (%)	pH	S_{BET}[a] ($m^2\ g^{-1}$)	V_{total}[b] ($cm^3\ g^{-1}$)	D_{ap}[c] (nm)
BC	29.1	11.2	9.94	0.50	ND[d]	ND
$AFFA_{200}$/BC	30.7	37.0	11.6	11.9	0.005	7.26
$AFFA_{200}$-NA/BC	34.3	33.5	9.36	83.6	0.014	14.0
$AFFA_{200}$-DW/BC	33.3	28.8	9.87	59.6	0.012	16.8
$AFFA_{600}$/BC	31.1	36.9	11.5	2.54	0.009	15.8
$AFFA_{600}$-NA/BC	34.6	28.7	9.71	50.5	0.011	23.9
$AFFA_{600}$-DW/BC	32.6	34.1	9.97	137	0.017	8.19

[a] Brunauer–Emmett–Teller (BET)-specific surface area; [b]Total pore volume; [c]Average pore diameter; [d]Not detected

BC and $AFFA_{600}$-NA/BC (34.3–34.6%) were higher than those of the other four AFFA/BC samples. These results are consistent with those of previous studies (Guo et al. 2012; Xu et al. 2020). Although NaOH remained in $AFFA_{200}$, the $AFFA_{200}$/BC yield (30%) was still higher than that of BC. This indicates that the Na^+ ions enter the AFFA/BC sample during pyrolysis, while C–Si and C–Al bonds form, which is in line with mass conservation laws (Wang et al. 2020).

Compared with pure BC, the ash contents of the AFFA/BC samples were 17.5–25.8% (wt%) higher. During co-pyrolysis, the remaining NaOH in $AFFA_{200}$ and $AFFA_{600}$ decomposed the organic matter in CS. Na and O were introduced after intermediate products (such as H_2O) evaporated during pyrolysis, and other products existed in the form of minerals in the solid residues, which increased the ash content of $AFFA_{200}$/BC and $AFFA_{600}$/BC (Table 1). The ash contents of $AFFA_{200}$-DW/BC (28.8%) and $AFFA_{600}$-NA/BC (28.7%) were relatively low. The S_{BET} values of the AFFA/BC samples were larger than that of BC (0.50 $m^2\ g^{-1}$). Among the AFFA/BC samples, the S_{BET} of $AFFA_{600}$-DW/BC (137 $m^2\ g^{-1}$) was the largest, and that of $AFFA_{200}$-NA/BC was approximately 84 $m^2\ g^{-1}$. However, the S_{BET} values of $AFFA_{200}$/BC and $AFFA_{600}$/BC were only 11.9 and 2.54 $m^2\ g^{-1}$, respectively, which was attributed to the collapse of their internal structures during co-pyrolysis owing to the remaining NaOH. Although the pH of CS was close to 5, the pH of the BC sample exceeded 9 owing to the release of alkali salts and the reduction of acidic surface functional groups during pyrolysis (Yuan et al. 2011; Zheng et al. 2013). When CS was directly co-pyrolyzed with $AFFA_{200}$ or $AFFA_{600}$, the alkalinity of the resulting AFFA/BC samples was affected by the remaining NaOH; thus, $AFFA_{200}$/BC and $AFFA_{600}$/BC had higher alkalinity.

The total C content of the pure BC sample was affected by carbonization and dehydration during pyrolysis, therefore it was approximately 33% (wt%) higher than that of CS (Table 2). The increase in the total C content was lower for the AFFA/BC samples (~9–23%) than that for BC, which was attributed to the decreased proportion of biomass. The total C contents of $AFFA_{200}$/BC (55.2%) and $AFFA_{600}$/BC (52.2%) were lower than those of the other four AFFA/BC samples (>60%). After high-temperature pyrolysis, the H and O contents of the BC sample were significantly decreased, the H/C atomic ratio decreased by 1.36, and the O/C atomic ratio decreased by approximately 0.47. These changes are caused by the decarboxylation, decarbonylation, and dehydration of the biomass during pyrolysis (Zhang et al. 2020). The decrease in the H/C, O/C, and (O + N)/C ratios also indicate the high aromaticity and low polarity of BC, which is attributed to the removal of polar surface functional groups and the carbonization of organic substances to form aromatic compounds during high-temperature pyrolysis. The decrease in the H and O contents was greater for the AFFA/BC samples than that for pure BC, indicating stronger decarboxylation, decarbonylation, and dehydration effects. In contrast, pyrolysis did not significantly affect the N contents of the BC and AFFA/BC samples, which is consistent with the results of previous studies (Ahmad et al. 2014). The $AFFA_{600}$/BC sample had the highest (O + N)/C and O/C ratios of 0.14 and 0.13, respectively, compared to 0.09 and 0.10, respectively, for BC. Thus, the $AFFA_{600}$/BC sample had highest polarity with hydrophilic behavior (Wang et al. 2020). In contrast, because washing with NA greatly reduced the content of O present as OH^- in $AFFA_{600}$, the $AFFA_{600}$-NA/BC sample had the lowest O content (2.70%) and low (O + N)/C and O/C ratios; therefore, it had the weakest polarity with hydrophobic behavior.

Table 2 Bulk and surface elemental characteristics of BC and AFFA/BC

Adsorbents	Bulk elemental composition (weight %)				Atomic ratio			Surface elemental composition (%)				
	C	N	H	O*	H/C	O/C	(O + N)/C	C	O	Si	Al	Na
BM	43.1	0.60	5.93	32.4	1.65	0.56	0.57	–	–	–	–	–
BC	76.5	0.95	1.82	9.47	0.29	0.09	0.10	87.7a	6.70a	1.04a	0.06b	0.03a
$AFFA_{200}$/BC	55.2	0.61	1.37	5.80	0.30	0.08	0.09	64.0ab	17.3a	4.41a	0.49b	6.79a
$AFFA_{200}$-NA/BC	60.5	0.80	1.27	3.93	0.25	0.05	0.06	22.4c	29.8a	20.7a	10.9a	4.91a
$AFFA_{200}$-DW/BC	62.1	0.73	1.36	7.00	0.26	0.08	0.09	44.6abc	20.4a	11.9a	6.09ab	3.28a
$AFFA_{600}$/BC	52.2	0.66	1.06	9.14	0.24	0.13	0.14	49.2abc	16.8a	6.96a	0.87ab	8.00a
$AFFA_{600}$-NA/BC	66.6	0.79	1.18	2.70	0.21	0.03	0.04	8.71c	19.3a	13.4a	7.98ab	4.62a
$AFFA_{600}$-DW/BC	60.2	0.64	1.16	3.90	0.23	0.05	0.06	33.0bc	29.4a	14.5a	7.79ab	5.96a

*Obtained by $\%O = 100\% - (\%C + \%N + \%H + \%S + \%\text{ash})$

Different letters indicate significant difference for the results in the same column

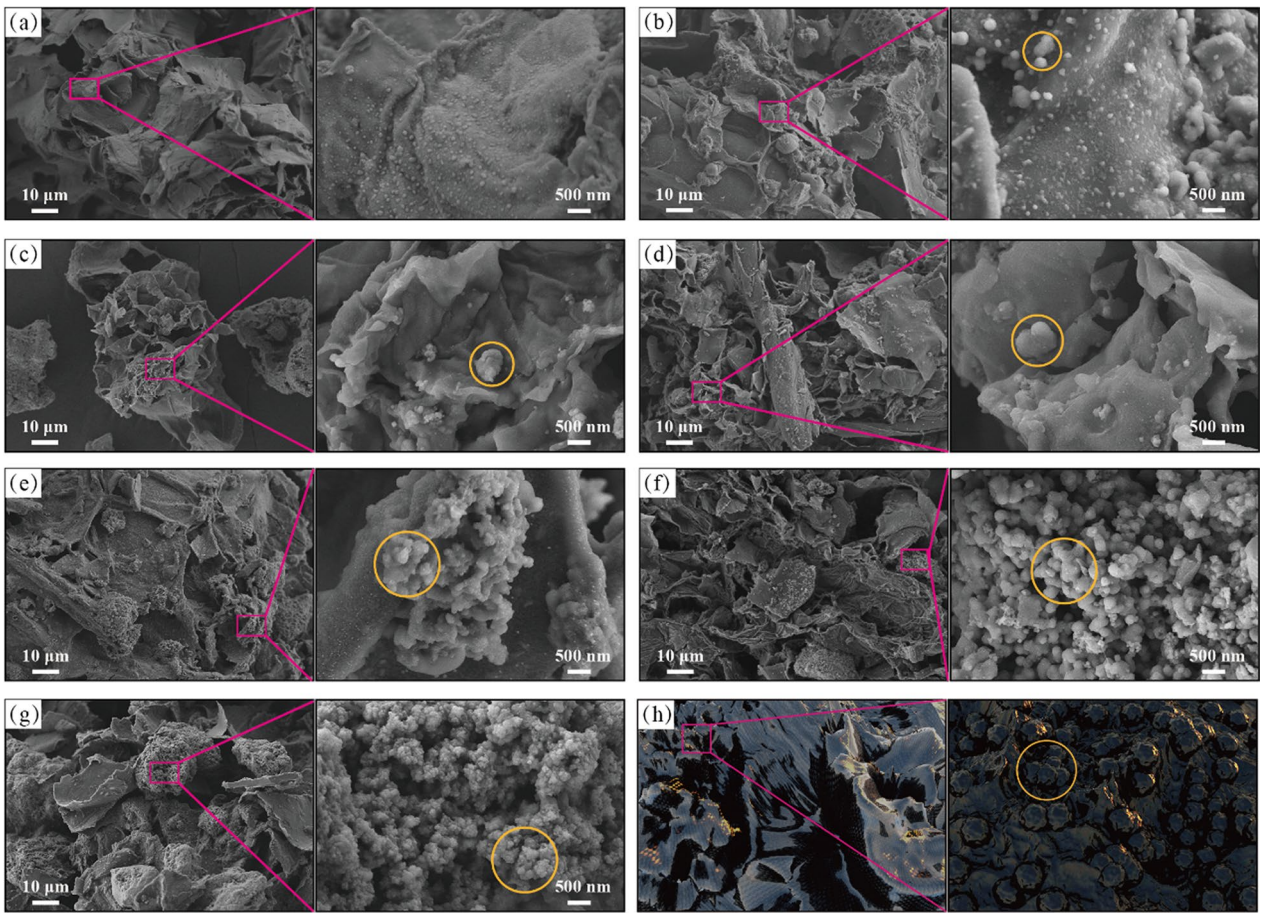

Fig. 2 SEM images of **a** BC and **b**–**g** AFFA/BC ($AFFA_{200}$/BC, $AFFA_{200}$-NA/BC, $AFFA_{200}$-DW/BC, $AFFA_{600}$/BC, $AFFA_{600}$-NA/BC, and $AFFA_{600}$-DW/BC, respectively); **h** structure modeling of AFFA/BC

SEM images of the BCs are shown in Fig. 2. The AFFA/BC samples had rougher surfaces than pure BC, with smooth convex substances (e.g., in the circular region) on the AFFA/BC surfaces. From the mineral composition of AFFA (Fig. 2), these observations are attributed to the aluminosilicate content of AFFA. The EDS spectra demonstrated that the major surface elements of BC were C and O (Table 2), whereas the AFFA/BC surface contained greater amounts of O, Na, Si, and Al. Therefore, we inferred that the main constituent elements of AFFA were successfully implanted in AFFA/BC. The $AFFA_{200}$/BC and $AFFA_{600}$/BC samples were highly alkaline (pH > 11), and their surface Na content was higher than that of the other four AFFA/BCs; however, their surface Si and Al contents were lower (Tables 1 and 2). This is ascribed to the residual NaOH in $AFFA_{200}$/BC and $AFFA_{600}$/BC, which aided the introduction of Na but was not conducive to the loading of Si and Al.

As listed in Table 1, the AFFA/BC samples had larger S_{BET}, V_{total}, and D_{avg} values than the pure BC sample. The highest S_{BET} value was exhibited by $AFFA_{600}$-DW/BC (137 $m^2\ g^{-1}$), followed by $AFFA_{200}$-NA/BC (83.6 $m^2\ g^{-1}$), $AFFA_{200}$-DW/BC (59.6 $m^2\ g^{-1}$), and $AFFA_{600}$-NA/BC (50.5 $m^2\ g^{-1}$). During the high-temperature pyrolysis of biomass, O and H are removed from the aromatic C–O, C = O ester, olefinic alkene–CH_2, and phenol–OH groups, resulting in an increase in the S_{BET} value (Chen et al. 2008; Tomczyk et al. 2020). In addition, volatile compounds are released during carbonization, which increases the pore size and number of internal pores, resulting in higher porosity. The Si–O and Al–O bonds in AFFA form stable chemical bonds such as C–Si and C–Al during co-pyrolysis, which prevents the internal structure from being affected by the release of volatile compounds during high-temperature treatment. Therefore, AFFA protects the BC structure from collapsing during pyrolysis.

On the other hand, the S_{BET} values of $AFFA_{200}$/BC (11.9 $m^2\ g^{-1}$) and $AFFA_{600}$/BC (2.54 $m^2\ g^{-1}$) were relatively low (Table 1). This is ascribed to the residual NaOH

in $AFFA_{200}$ and $AFFA_{600}$, which reacts with the chemical components of CS during high-temperature pyrolysis, producing many gases (e.g., H_2, CO, and CO_2) that reduce the structural stability and result in the collapse of the internal structure of BC (Sajjadi et al. 2019). Although new micropores appeared on the surface of these samples, their internal pore structures were blocked by the formation of products such as Na_2O, decreasing their S_{BET} values, as shown by Huang et al. (2020a).

Additional file 1: Fig. S3 shows the pore size distribution of the AFFA/BC samples. The samples were mainly mesoporous with some micropores, except for $AFFA_{600}$/BC, which did not contain micropores. The alkali/sodium salt in AFFA reacts with the activated carbon atoms in BC to generate CO_2 and other gases, which results in the formation of micropores and thus greatly enhances the porosity of the AFFA/BC samples (Table 1).

Figure 3 shows the FTIR spectra of the BC and AFFA/BC samples. The broad peak at ~ 3433 cm^{-1} is ascribed to the stretching vibrations of alcoholic and phenolic –OH groups involved in intermolecular hydrogen bonding. The peak at 1452 cm^{-1} corresponds to the shear bending vibrations of $-CH_2$. The slight C = O (with conjugation) stretching vibrations, denoted by the peak at 1629 cm^{-1}, indicate the existence of carboxylic compounds on the surface of BC and AFFA/BC (Gao et al. 2019a; Li and McDonald 2014). The higher intensity of the ~ 1028 cm^{-1} peak of the AFFA/BC samples (except for $AFFA_{200}$/BC) compared with that of BC indicates stronger C–O vibrations owing to the protection by AFFA of functional groups from high-temperature damage. The stretching peaks of Si–O or Al–O at 704 and 470 cm^{-1} confirm that SiO_2 or Al_2O_3 in AFFA were successfully loaded onto the AFFA/BC surface (Han et al. 2017; Qian and Chen 2013). These results indicate that oxygen-containing groups (–OH and $-COO^-$) and mineral fractions (e.g., SiO_3^{2-}, a SiO_2 component) were present simultaneously in AFFA/BC, which is consistent with previous results (Han et al. 2017; Qian and Chen 2013Wang KF et al. 2020). Therefore, AFFA/BC can be used to adsorb Pb(II) through precipitation and the complexation of functional groups, which is expected to increase the adsorption capacity compared to pure BC.

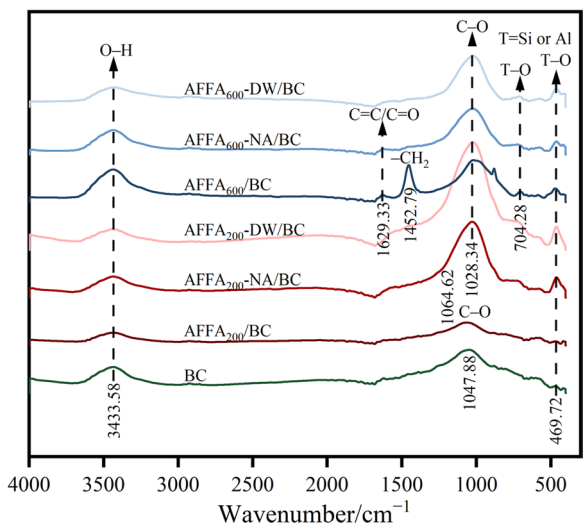

Fig. 3 FTIR spectrum of BC and AFFA/BC

3.2 Pb(II) adsorption characteristics

3.2.1 Effect of initial pH

Figure 4a depicts the effect of pH (3–6) on the Pb(II) adsorption performance of the BC and AFFA/BC samples under the adsorbent dosages of 1.0 g L^{-1} and the initial Pb(II) concentration of 20 mg L^{-1}. The Pb(II) adsorption capacity of each sample decreased slightly with increasing pH. Notably, the Pb(II) adsorption capacities of the $AFFA_{200}$/BC, $AFFA_{200}$-NA/BC, and $AFFA_{600}$/BC samples (> 22 mg g^{-1}) were higher than that of BC under all conditions, and significantly higher than those of partial BC samples reported previously (Wang et al. 2015a, 2015b; Zama et al. 2017). $AFFA_{200}$-NA/BC presented the highest Pb(II) adsorption capacity (23.26 mg g^{-1}) at pH 3. At pH 4–6, the equilibrium adsorption capacities of the AFFA/BC samples were all higher than that of BC. However, at pH 3, the Pb(II) adsorption capacities of $AFFA_{200}$-DW/BC, $AFFA_{600}$-NA/BC, and $AFFA_{600}$-DW/BC were lower than that of BC (< 21 mg g^{-1}), with $AFFA_{200}$-DW/BC exhibiting the weakest Pb(II) adsorption capacity (14.69 mg g^{-1}).

As shown in Fig. 4b, the final pH of all adsorbent–adsorbate mixtures exceeded their initial pH, and protonation occurred on the surface of the adsorbents (BC and AFFA/BC), with the surface being positively charged within the chosen pH range (3–6) (Huang et al. 2020a; Kołodyńska et al. 2016). Therefore, the poor adsorption performance of $AFFA_{200}$-DW/BC, $AFFA_{600}$-NA/BC, and $AFFA_{600}$-DW/BC at an initial pH of 3 was ascribed to the large concentration of solute H^+ ions, which compete with Pb(II) and $[Pb(H_2O)_6]^{2+}$ (a hydrated ion of Pb) for adsorption sites, as well as the lowered deprotonated state of the surface carboxylic compounds (–COOH and –COONa), in line with previous studies (Cai et al. 2021a; Kołodyńska et al. 2012; Shen et al. 2021; Wu et al. 2021; Yang et al. 2014). As the pH increased, the solute $[Pb(H_2O)_6]^{2+}$ ions were converted to $[Pb(OH)_6]^{4-}$ ions; this decreased the competition of Pb(II) with other protons for the adsorption sites, which was conductive to Pb(II) adsorption. In addition, the SiO_2 groups on the surface of AFFA/BC become negatively charged as the pH increases (Han et al. 2017). Therefore, increasing the

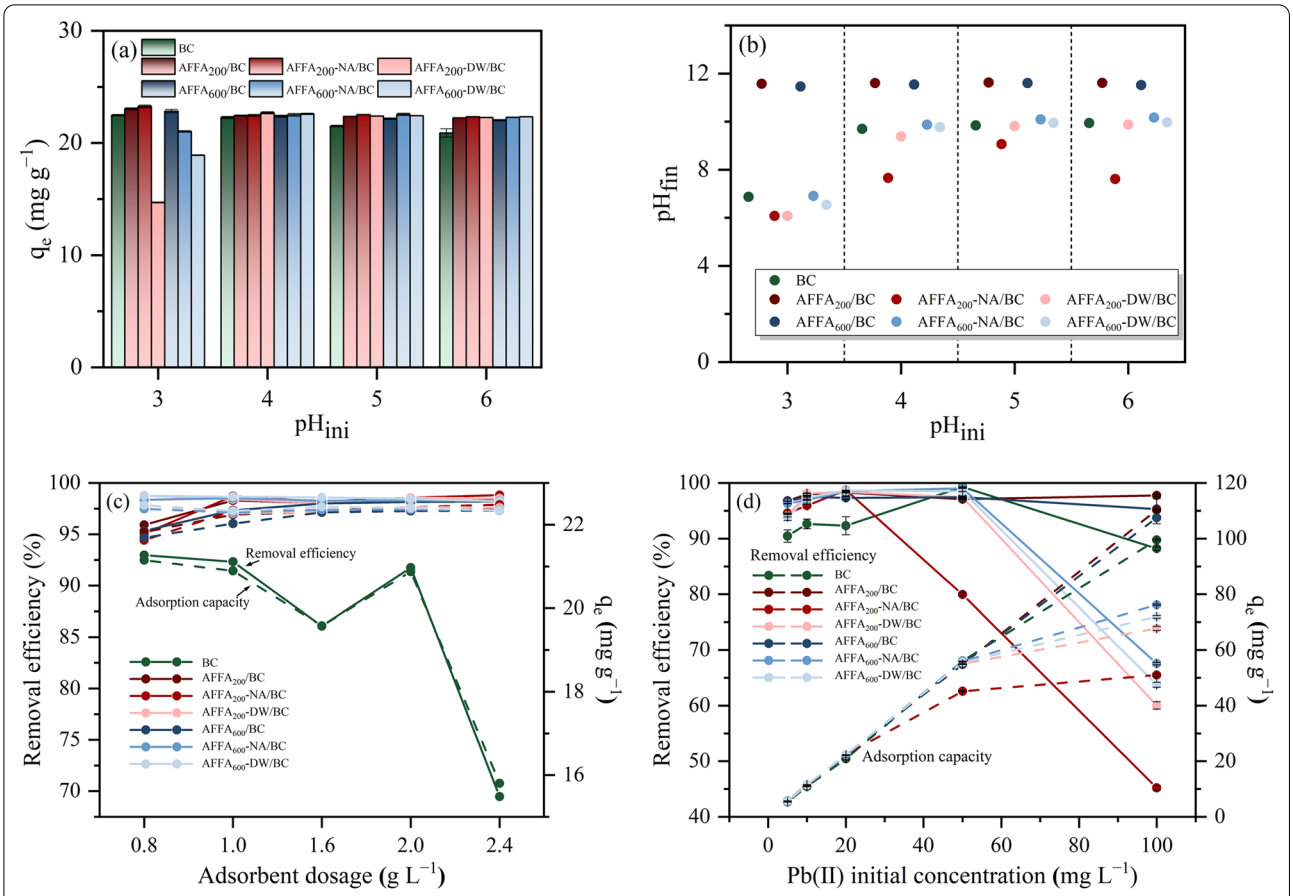

Fig. 4 Influence of **a** initial solution pH on the Pb(II) adsorption capacity of BC and AFFA/BC and **b** solution pH before and after adsorption; Pb(II) adsorption by BC and AFFA/BC at **c** different dosages and **d** initial concentrations

pH could activate these adsorption sites, leading to their complete occupancy by Pb(II). Furthermore, the adsorbent surface was deprotonated owing to the pH increase, facilitating the complexation of surface functional groups ($-COOH^-$) with Pb(II). These results infer that AFFA/BC is suitable for treating acidic wastewater at pH 4–6. Under strongly acidic conditions (initial pH of 3), the final pH of the adsorbent–adsorbate mixture reached between 6 and 7 at adsorption equilibrium. However, owing to the high alkalinity of the $AFFA_{200}$/BC and $AFFA_{600}$/BC samples, the pH of these adsorbent–adsorbate mixtures was above 11 once adsorption equilibrium was reached. In contrast to the results of Shen et al. (2021), as the initial solution pH increased, the pH of the equilibrium adsorbent–adsorbate mixture increased to approximately 8–10 owing to the different reactivities of the surface functional groups (–OH, –COO, and Si–O) under different initial pH conditions. The pH of the solution after adsorption by $AFFA_{200}$-NA/BC was relatively low, which was attributed to the low pH of the adsorbent.

3.2.2 Effect of adsorbent dosage

Figure 4c shows the changes in the Pb(II) removal efficiency and adsorption capacity under the initial solution pH of ~ 5 and the initial Pb(II) concentration of 20 mg L^{-1} with different dosages of adsorbent (0.8–2.4 g L^{-1}). The Pb(II) removal efficiency of BC was below 93% and decreased with an increase in the BC dosage owing to agglomeration. In contrast, the Pb(II) removal efficiencies of the AFFA/BC samples at 0.8–2.4 g L^{-1} were all above 95%. Although the AFFA/BC samples were alkaline and their soluble OH^- could precipitate with Pb(II), the surfaces of the samples were loaded with Na^+ ions, which enabled Pb(II) adsorption via cation exchange (Yang et al. 2019; Zhang et al. 2019). Similar results have been reported for NaOH-modified BC (Ding et al. 2016; Mahdi et al. 2019).

When the dosages of $AFFA_{200}$/BC, $AFFA_{200}$-NA/BC, and $AFFA_{600}$/BC increased from 0.8 to 1.6 g L^{-1}, their Pb(II) removal efficiencies increased by more than 2%, and their Pb(II) adsorption capacities reached 22 mg g^{-1}. This enhanced Pb(II) adsorption performance

is attributed to the developed pore structure, rich surface functional groups, and a lot of adsorption sites of these adsorbents (Table 1 and Fig. 3). The Pb(II) removal efficiencies and equilibrium adsorption capacities of the other three AFFA/BC samples were negligibly affected by dosage and remained above 98% and 22 mg g^{-1}, respectively. Considering the Pb(II) adsorption capacity and economic benefits of the BC samples, 1.0 g L^{-1} was selected as the optimal dosage.

3.2.3 Effect of initial Pb(II) concentration

The influence of the initial Pb(II) concentration (5–100 mg L^{-1}) on the adsorption performance of BC and AFFA/BC under the adsorbent dosage of 1.0 g L^{-1} and the initial solution pH of ~ 5 is shown in Fig. 4d. For $AFFA_{200}$/BC, the adsorption capacity increased nonlinearly with Pb(II) concentration, reaching the highest adsorption capacity of 110.29 mg g^{-1} at a Pb(II) concentration of 100 mg L^{-1}. Notably, this is approximately 10% higher than that of BC under the same adsorption conditions. As the initial Pb(II) concentration increased from 5 to 20 mg L^{-1}, the Pb(II) removal efficiencies of all the AFFA/BC samples increased. At 20 mg L^{-1}, the Pb(II) removal efficiencies and adsorption capacities were 97.34–98.71% and 22.03–22.34 mg g^{-1}, respectively. Upon increasing the Pb(II) concentration to 50 mg L^{-1}, the Pb(II) removal efficiencies were maintained or decreased slightly, which was attributed to the high alkalinity of all the AFFA/BC samples (Table 1). Upon further increasing the initial Pb(II) concentration to 100 mg L^{-1}, the Pb(II) removal efficiency of $AFFA_{200}$/BC remained mostly unchanged, while that of $AFFA_{600}$/BC decreased by 2.14%. The Pb(II) removal performance of the other four AFFA/BCs was significantly reduced upon increasing the initial Pb(II) concentration from 50 to 100 mg L^{-1}. When the AFFA/BC adsorption sites were saturated, the excess Pb(II) could not be adsorbed and remained in solution. The enhanced ionic strength at high Pb(II) concentrations led to more aggregation of the adsorbents, resulting in decreased availability of the binding sites on the adsorbents and thus a decline in the Pb(II) adsorption capacity. Similar findings have been reported for the adsorption of Pb(II) on BC from CS modified by other chemicals (Du et al. 2020; Fan et al. 2020).

3.2.4 Correlation analysis of basic characteristics and adsorption capacity

The correlations between the basic characteristics of the AFFA/BC samples and their equilibrium Pb(II) adsorption capacities were investigated. As shown in Fig. 5, the ash content and O, Si, Al, and Na contents of the AFFA/BC samples were positively correlated with the equilibrium Pb(II) adsorption capacity. The concentration of surface O and Na significantly affected the Pb(II) adsorption by AFFA/BC. The O content correlates to the number of oxygen-containing functional groups, which facilitate the chemical adsorption of Pb(II). In addition, an increased Na content enhanced the cation exchange capacity of AFFA/BC (Gao et al. 2019b; Trakal et al. 2014). However, the Pb(II) adsorption on the $AFFA_{200}$-NA/BC and $AFFA_{600}$-DW/BC samples was enhanced by their increased S_{BET} and V_{total} values (Table 1).

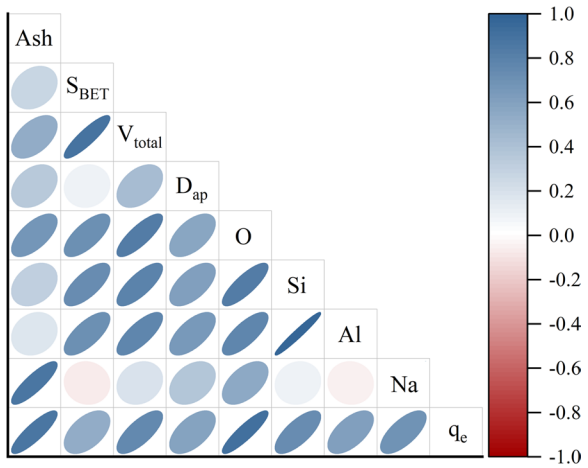

Fig. 5 Correlation of basic properties of BC or AFFA/BC with equilibrium adsorption capacity of Pb(II) (temperature = 25 ℃; pH ≈ 5; Pb(II) initial concentration = 20 mg L^{-1}; dosage = 1.0 g L^{-1}; time = 24 h)

3.3 Adsorption kinetics and isotherms

3.3.1 Adsorption kinetics

Figure 6a shows the adsorption behavior of the BC and AFFA/BC samples as a function of contact time. Between 200 and 1440 min, the Pb(II) adsorption capacity of AFFA/BC changed slowly and gradually plateaued. Kinetic models were used to simulate the adsorption of Pb(II) from the liquid phase to the solid phase. The adsorption data were fitted to the PFO, PSO, and IPD models (Additional file 1: Equations S2–S4), as shown in Fig. 6b, c. The model parameters are listed in Additional file 1: Table S3.

The PSO model described the adsorption data more accurately than the PFO model based on their correlation coefficients (R^2, Additional file 1: Table S3). Therefore, Pb(II) adsorption by AFFA/BC may involve multiple adsorption mechanisms. Except for $AFFA_{200}$/BC and $AFFA_{600}$/BC, the equilibrium Pb(II) adsorption capacities calculated by the PSO adsorption method were mostly consistent with the experimental results, demonstrating that the adsorption systems reached equilibrium.

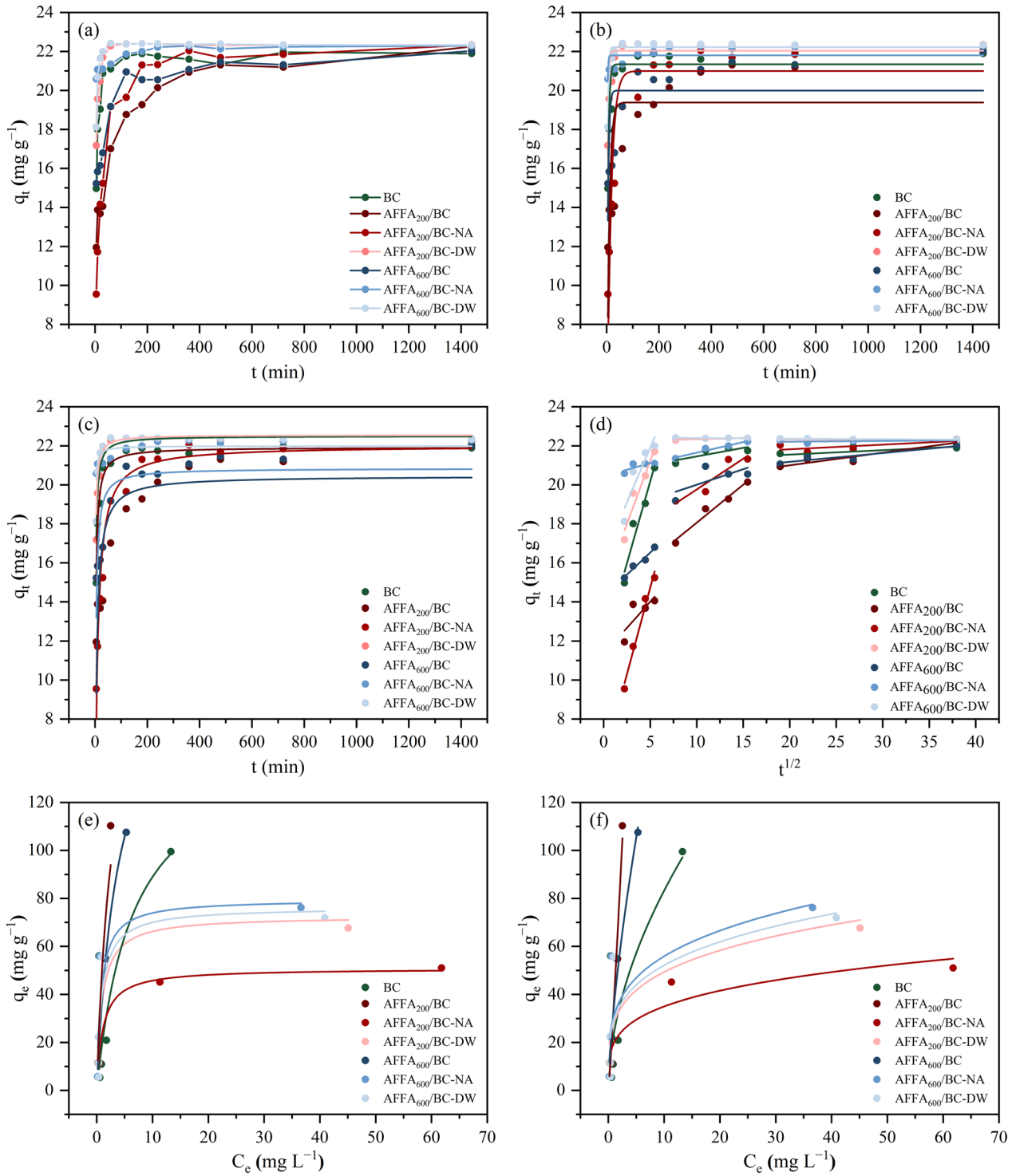

Fig. 6 **a** Influence of contact time on Pb(II) adsorption; **b** pseudo-first-order kinetic model; **c** pseudo-second-order kinetic model; **d** intra-particle diffusion model fitting curves of Pb(II) removal by BC and AFFA/BC (Pb(II) initial concentration = 20 mg L^{-1}, dosage = 1.0 g L^{-1}, pH ≈ 5, and temperature = 25 ℃); **e** Langmuir and **f** Freundlich adsorption isotherms of different BCs for Pb(II) adsorption (dosage = 1.0 g L^{-1}, pH ≈ 5, temperature = 25 ℃, and time = 24 h)

Wang et al. (2015c) calculated the equilibrium Pb(II) adsorption capacities of three kinds of BC prepared from pine wood feedstock based on the PSO model, with the results ranging from 2.15 to 17.50 mg g^{-1}. These values are lower than the Pb(II) adsorption capacities achieved by the AFFA/BC samples in this study. Furthermore, Pb(II) chemical adsorption of AFFA/BC samples was the main rate-controlling step, which might be related to ion exchange between the adsorbate and the adsorbent (Rangabhashiyam et al. 2022). The PSO model had a relatively poor fit to the Pb(II) adsorption data of the $AFFA_{200}$/BC and $AFFA_{600}$/BC samples, which might be attributed to the presence of residual NaOH in these materials. The OH^- and SiO_3^{2-} groups on the surface of $AFFA_{200}$/BC and $AFFA_{600}$/BC could also react with Pb(II) to form precipitates, which would affect the Pb(II) adsorption data, leading to a poor fit of the model.

To elucidate the Pb(II) adsorption mechanism of AFFA/BC and determine the rate-controlling steps, the IPD model was fitted to the equilibrium data. Figure 6d shows q_t (the adsorption amount at time t) as a function of $t^{0.5}$ (Additional file 1: Eq. S4). The IPD model could not fit the entire experimental range; therefore, the adsorption process was divided into three stages. The first stage (0–30 min) had a high adsorption rate; therefore, this stage corresponded to surface adsorption. The second stage (60–240 min) involved slow adsorption or IPD, as Pb(II) began to diffuse into the inner pores of the adsorbent. The third stage (360–1440 min) corresponded to equilibrium adsorption, during which the solute Pb(II) concentration was lower and the diffusion of particles began to slow down. The Pb(II) uptake during the third stage was mainly controlled by an interplay of physical and chemical adsorption, ion exchange, precipitation, and complexation (Qiu et al. 2018). As shown in Fig. 6d and Additional file 1: Table S3, Pb(II) adsorption was not only affected by surface adsorption and IPD but also by chemical adsorption and ion exchange, as evidenced by the non-negligible C (the constant governing boundary layer and thickness, mg g^{-1}) constants of the IPD model (Additional file 1: Table S3) (Gundogdu et al. 2012; Kong et al. 2016).

3.3.2 Adsorption isotherms

The Langmuir and Freundlich models were used to fit the Pb(II) adsorption data at 25 °C, and the results are shown in Fig. 6e, f. According to the R^2 values (Additional file 1: Table S4), the Langmuir model ($R^2 = 0.73–0.99$) fitted the AFFA/BC adsorption data better than the Freundlich model ($R^2 = 0.66–0.98$), indicating that Pb(II) adsorption on AFFA/BC was similar to monolayer chemisorption (Liu et al. 2022). $AFFA_{200}$/BC presented the highest calculated adsorption capacity at equilibrium (q_{max}) of 201.66 mg g^{-1}, followed by $AFFA_{600}$/BC (186.81 mg g^{-1}). The q_m values of the other four AFFA/BC samples were all below 80 mg g^{-1}, while that of BC was 145.98 mg g^{-1}. The theoretical results calculated using the Langmuir model were in agreement with the experimental results in Sect. 3.2.3, that is, $AFFA_{200}$/BC and $AFFA_{600}$/BC showed the strongest Pb(II) adsorption capacities at high initial Pb(II) concentrations. R_L is a parameter of the Langmuir adsorption isotherm that can describe the rudimentary characteristics of the model (Teng et al. 2020). The R_L value is calculated by the equation $R_L = 1/(1 + K_L C_0)$, where K_L is the adsorption constant of the Langmuir model and C_0 is the initial concentration of the solution; therefore, R_L has a negative correlation with C_0 (Additional file 1: Fig. S4). The R_L values of the AFFA/BC samples were between 0 and 1, indicating favorable adsorption. The R_L value of $AFFA_{600}$-NA/BC was close to 0, indicating that Pb(II) adsorption was irreversible (Nguyen et al. 2019; Yang et al. 2013). In addition, the R_L values of the AFFA/BC samples were lower than that of BC, implying a higher affinity for Pb(II).

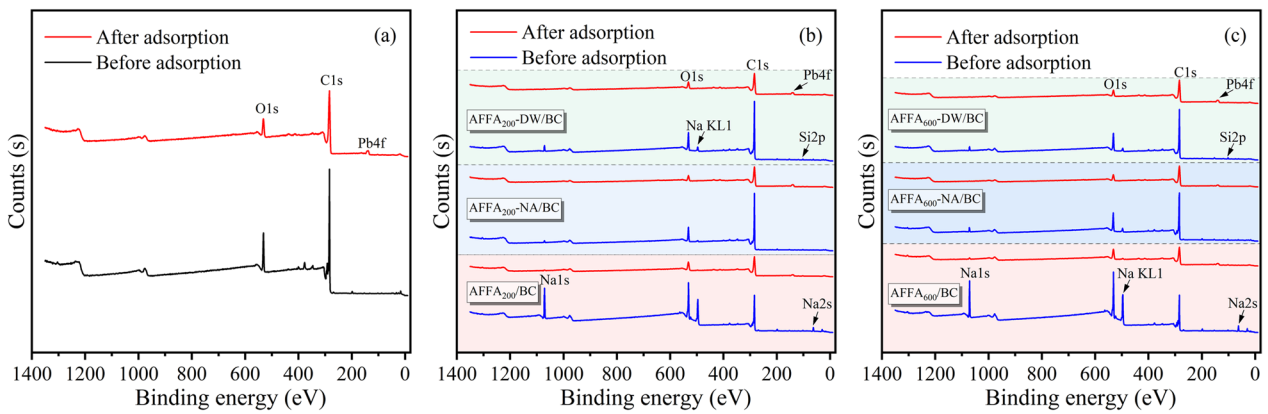

Fig. 7 XPS spectra of **a** BC and **b**, **c** AFFA/BC before and after Pb(II) adsorption

3.4 Adsorption mechanism

Figure 7 shows the full XPS scans of the BC and AFFA/BC samples before and after Pb(II) adsorption. The spectra contained strong Pb 4f peaks at ~ 140 eV after Pb(II) adsorption, demonstrating that Pb(II) was successfully adsorbed onto the adsorbent surfaces. In addition, the spectra of all the AFFA/BC samples before Pb(II) adsorption contained strong Na 1 s peaks at ~ 1071.28 eV and weak Si 2p peaks at ~ 102 eV, which indicate the significant Na^+ loading after the co-pyrolysis of biomass and AFFA, consistent with the EDS results (Table 2). After adsorption, the Na 1 s peak mostly disappeared, indicating that some Pb(II) adsorption by AFFA/BC was achieved by Na^+ cation exchange. This is in line with previous reports of Pb(II) adsorption by AFFA (Huang et al. 2020b). The O 1 s peaks of $AFFA_{200}$/BC and $AFFA_{600}$/BC were weaker than those of the other four AFFA/BCs. This was attributed to their high alkalinity and enhanced decarboxylation, decarburization, and dehydration during pyrolysis, which is consistent with the results of the correlation analysis (Fig. 5). The reduced O 1 s peak of the AFFA/BC samples following Pb(II) adsorption was ascribed to surface OH^- and SiO_3^{2-} groups precipitating with heavy metal ions, which triggered the detachment of some O atoms (Huang et al. 2020b; Zhao et al. 2020b).

To further understand the microscopic interactions between AFFA/BC and Pb(II), the C 1 s and O 1 s XPS spectra before and after adsorption were analyzed (Additional file 1: Fig. S5). The C 1 s spectra of BC and AFFA/BC could be deconvolved into three peaks corresponding to O–C=O, C–O, and C–C/C=C/C–H. Before adsorption, these peaks for $AFFA_{200}$-NA/BC were at binding energies of 288.81, 284.41, and 283.54 eV, respectively (Additional file 1: Fig. S5c). However, the peak positions shifted to higher binding energies of 289.24, 285.48, and 283.58 eV, respectively, after Pb(II) adsorption, implying that the adsorption process was controlled by surface complexation (Huang et al. 2020b; Pang et al. 2018). A similar observation was made for the BC and other AFFA/BC samples. The surface of $AFFA_{200}$-NA/BC, $AFFA_{200}$-DW/BC, and $AFFA_{600}$-NA/BC exhibited more abundant C–C/C=C/C–H chemical bonds than that of BC (Additional file 1: Fig. S5c, d, f), which greatly stabilized their structures. After Pb(II) adsorption, the number of C–C/C=C/C–H bonds on the surface of the $AFFA_{200}$-NA/BC and $AFFA_{200}$-DW/BC samples were significantly reduced owing to their high adsorption capacities (Fig. 4).

Additional file 1: Fig. S5a′–g′ show the O 1 s XPS spectra of the BC and AFFA/BC samples before and after Pb(II) adsorption. Based on the different oxygen bonds, the O 1 s XPS spectra of the AFFA/BC samples were deconvolved into four peaks corresponding to O–C=O, C–O/O–H, C=O, and Si–O, while that of BC was deconvolved into three peaks corresponding to O–C=O, C–O/O–H, and C=O (Cai et al. 2021b; Deng et al. 2016; Pang et al. 2018). The areas of the O–C=O (carboxyl), C–O/O–H, and C=O (esters, anhydrides) peaks decreased after Pb(II) adsorption, indicating that the carboxyl groups participated in Pb(II) adsorption, which was in agreement with the FTIR results. The narrow-spectrum XPS scans of Pb 4f on the BC and AFFA/BC surfaces are shown in Additional file 1: Fig. S6; $AFFA_{200}$-NA/BC, $AFFA_{200}$-DW/BC, and $AFFA_{600}$-DW/BC exhibited larger Pb(II) adsorption capacities than the other samples.

Based on the adsorption kinetics, isothermal adsorption characteristics, and full- and narrow-spectrum (C 1 s, O 1 s, and Pb 4f) XPS scans of BC and AFFA/BC before and after adsorption, the proposed mechanism of Pb(II) adsorption on the AFFA/BC samples (Fig. 8) mainly involves physical adsorption, precipitation, cation exchange, and complexation. The pore structure of AFFA/BC was well developed (Table 1 and Fig. 2); therefore, the physical adsorption of Pb(II) was enhanced. The OH^- and SiO_3^{2-} groups on the surface of AFFA/BC could precipitate with Pb(II), thereby removing it from solution (Han et al. 2017). In line with previous studies (Han et al. 2017; Qian and Chen 2013; Wang et al. 2020), AFFA/BC also achieved Pb(II) adsorption through cation exchange of Na^+ and complexation owing to the presence of –OH, $–COO^-$, and Si–O.

4 Conclusions

In this study, AFFA/BCs were prepared by the co-pyrolysis of CS and AFFA and used to remove Pb(II) from water. The BC yield, ash content, pH, and S_{BET} values of the AFFA/BC samples were higher than those of pure

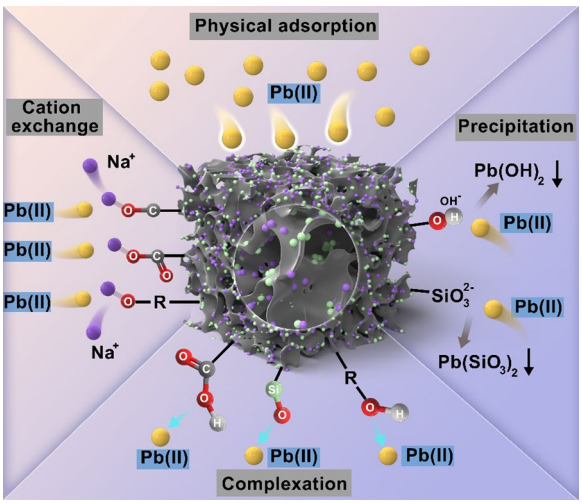

Fig. 8 Proposed mechanisms of interaction between AFFA/BC and Pb(II)

BC, while the Na, Si, and Al contents on the AFFA/BC surface were significantly higher than those on the BC surface. In addition, fine particles (e.g., sodium aluminosilicate) were present on the AFFA/BC surface. The number of C–O bonds on the AFFA/BC surface increased and new chemical bonds such as Si–O and Al–O were formed, indicating that the main constituents of AFFA were successfully imparted in AFFA/BC. The maximum theoretical Pb(II) adsorption capacity of $AFFA_{200}$/BC (201.66 mg g^{-1}) was significantly higher than that of BC (145.98 mg g^{-1}), which was attributed to the large S_{BET} value, high cation (Na^+) exchange, increased number of oxygen-containing functional groups (–OH and $–COO^–$), and the complexation of Si components in AFFA/BC. Moreover, the AFFA/BC samples were more alkaline than BC and suitable for Pb(II) adsorption from acidic wastewater. The adsorption kinetics and isothermal adsorption of Pb(II) were simulated, indicating that Pb(II) adsorption by AFFA/BC was similar to monolayer chemisorption, while chemical adsorption was the main rate-controlling step. According to the XPS scans before and after adsorption, the main adsorption mechanisms of Pb(II) on AFFA/BC were precipitation with surface $OH^–$ and $SiO_3^{2–}$ groups; cation exchange with surface Na^+ ions; and complexation by Si–O, phenolic –OH, and $–COO^–$. This study provides a basis for the use and further investigation of AFFA/BC materials for the adsorption of Pb(II) and other heavy metal ions. In addition, it provides a theoretical basis for the application of modified BC adsorbents for wastewater treatment.

Abbreviations

AFFA: Alkali-fused fly ash; BC: Biochar; BET: Brunauer–Emmett–Teller; CS: Corn stalk; DW: Deionized water; EDS: Energy-dispersive X-ray spectroscopy; FA: Fly ash; FTIR: Fourier-transform infrared spectroscopy; IPD: Intraparticle diffusion; PFO: Pseudo-first-order; PSO: Pseudo-second-order; SEM: Scanning electron microscopy; TGA: Thermogravimetric analysis; XPS: X-ray photoelectron spectroscopy; XRD: X-ray diffraction.

Supplementary Information

The online version contains supplementary material available at https://doi.org/10.1007/s42773-022-00189-4.

Additional file 1. Text S1. Bulk elemental compositions. **Text S2.** Adsorption kinetics. **Text S3.** Adsorption isotherms. **Table S1.** Detection of potential metals and polycyclic aromatic hydrocarbons in FA. **Table S2.** Porous structural parameters of FA and AFFA. **Table S3.** Kinetic parameters of Pb(II) adsorption by BC and AFFA/BC. **Table S4.** Basic parameters of Langmuir and Freundlich adsorption isotherms. **Fig. S1.** Aperture distribution of **a** FA, **b** $AFFA_{200}$, and **c** $AFFA_{600}$. **Fig. S2. a** N_2 adsorption–desorption isotherms of FA, $AFFA_{200}$, and $AFFA_{600}$; X-ray diffraction patterns of **b** FA, **c** $AFFA_{200}$, and **d** $AFFA_{600}$; thermogravimetric analysis of raw fly ash (FA) and alkali-fused fly ash ($AFFA_{200}$ and $AFFA_{600}$): **e** TG (%) and **f** TGA (% min^{-1}) curves. **Fig. S3.** Pore size distribution map of AFFA/BC. **Fig. S4.** Correlation between R_L (a parameter of the Langmuir adsorption isotherm) and C_0 (initial Pb(II) concentration) values. **Fig. S5.** XPS spectra of the element scan of C1*s* and O1*s* in BC (**a** and **a′**) , $AFFA_{200}$/BC (**b** and **b′**), $AFFA_{200}$-NA/BC (**c** and **c′**), $AFFA_{200}$-DW/BC (**d** and **d′**), $AFFA_{600}$/BC (**e** and **e′**), $AFFA_{600}$-NA/BC (**f** and **f′**), and $AFFA_{600}$-DW/BC (**g** and **g′**) before and after Pb(II) adsorption. **Fig. S6**. XPS spectra region of Pb4f after Pb(II) adsorption by BC and AFFA/BC (**a**–**g**: BC, $AFFA_{200}$/BC, $AFFA_{200}$-NA/BC, $AFFA_{200}$-DW/BC, $AFFA_{600}$/BC, $AFFA_{600}$-NA/BC, and $AFFA_{600}$-DW/BC, respectively).

Acknowledgements

Yan Ma is grateful to the China Scholarship Council for supporting her study at UMass Amherst for one year.

Author contributions

Conceptualization: YM; Methodology: YM; Formal analysis and investigation: XY, YZ, and BC; Writing—original draft preparation: XY; Writing—review and editing: YM, HZ, and BX; Funding acquisition: YM. All authors read and approved the final manuscript.

Funding

This work was supported by the National Key Research and Development Program of China (Grant Number 2020YFC1806500).

Data availability

The data that support the findings of this study are available from the corresponding author upon request.

Declarations

Competing interests

The authors declare that they have no known competing financial interests or personal relationships that could have influenced the work reported in this paper.

Author details

[1]School of Chemical and Environmental Engineering, China University of Mining and Technology, Beijing 100083, China. [2]Institute of Coastal Environmental Pollution Control, Key Laboratory of Marine Environment and Ecology, Ministry of Education, Frontiers Science Center for Deep Ocean Multispheres and Earth System, Ocean University of China, Qingdao 266100, China. [3]Stockbridge School of Agriculture, University of Massachusetts, Amherst, MA 01003, USA.

Received: 24 January 2022 Revised: 7 November 2022 Accepted: 12 November 2022
Published online: 09 December 2022

References

Agarwal S, Rani A (2017) Adsorption of resorcinol from aqueous solution onto CTAB/NaOH/flyash composites: equilibrium, kinetics and thermodynamics. J Environ Chem Eng 5:526–538. https://doi.org/10.1016/j.jece.2016.11.035

Ahmad M, Rajapaksha AU, Lim JE, Zhang M, Bolan N, Mohan D, Vithanage M, Lee SS, Ok YS (2014) Biochar as a sorbent for contaminant management in soil and water: a review. Chemosphere 99:19–33. https://doi.org/10.1016/j.chemosphere.2013.10.071

Ahmad M, Ahmad M, Usman ARA, Al-Faraj AS, Abduljabbar A, Ok YS, Al-Wabel MI (2019) Date palm waste-derived biochar composites with silica and zeolite: synthesis, characterization and implication for carbon stability and recalcitrant potential. Environ Geochem Health 41:1687–1704. https://doi.org/10.1007/s10653-017-9947-0

Ameh AE, Musyoka NM, Fatoba OO, Syrtsova DA, Teplyakov VV, Petrik LF (2016) Synthesis of zeolite NaA membrane from fused fly ash extract. J Environ Sci Health A Tox Hazard Subst Environ Eng 51:348–356. https://doi.org/10.1080/10934529.2015.1109410

Bhagath Singh GVP, Subramaniam KVL (2016) Quantitative XRD study of amorphous phase in alkali activated low calcium siliceous fly ash. Constr Build Mater 124:139–147. https://doi.org/10.1016/j.conbuildmat.2016.07.081

Cai T, Du HH, Liu X, Tie BQ, Zeng ZX (2021a) Insights into the removal of Cd and Pb from aqueous solutions by NaOH– EtOH-modified biochar. Environ Technol Innov 24:102031. https://doi.org/10.1016/j.eti.2021.102031

Cai T, Liu XL, Zhang JC, Tie BQ, Lei M, Wei XD, Peng O, Du HH (2021b) Silicate-modified oiltea camellia shell-derived biochar: a novel and cost-effective sorbent for cadmium removal. J Clean Prod 281:125390. https://doi.org/10.1016/j.jclepro.2020.125390

Chang JN, Zhang HB, Cheng HY, Yan YY, Chang MC, Cao YZ, Huang F, Zhang GS, Yan M (2020) Spent *Ganoderma lucidum* substrate derived biochar as a new bio-adsorbent for Pb^{2+}/Cd^{2+} removal in water. Chemosphere 241:125121. https://doi.org/10.1016/j.chemosphere.2019.125121

Chen BL, Zhou DD, Zhu LZ (2008) Transitional adsorption and partition of nonpolar and polar aromatic contaminants by biochars of pine needles with different pyrolytic temperatures. Environ Sci Technol 42:5137–5143. https://doi.org/10.1021/es8002684

Cinperi NC, Ozturk E, Yigit NO, Kitis M (2019) Treatment of woolen textile wastewater using membrane bioreactor, nanofiltration and reverse osmosis for reuse in production processes. J Clean Prod 223:837–848. https://doi.org/10.1016/j.jclepro.2019.03.166

Deng S, Shu Y, Li SG, Tian G, Huang JY, Zhang F (2016) Chemical forms of the fluorine, chlorine, oxygen and carbon in coal fly ash and their correlations with mercury retention. J Hazard Mater 301:400–406. https://doi.org/10.1016/j.jhazmat.2015.09.032

Ding ZH, Hu X, Wan YS, Wang SS, Gao B (2016) Removal of lead, copper, cadmium, zinc, and nickel from aqueous solutions by alkali-modified biochar: batch and column tests. J Ind Eng Chem 33:239–245. https://doi.org/10.1016/j.jiec.2015.10.007

Du Q, Zhang SS, Song JP, Zhao Y, Yang F (2020) Activation of porous magnetized biochar by artificial humic acid for effective removal of lead ions. J Hazard Mater 389:122115. https://doi.org/10.1016/j.jhazmat.2020.122115

Fan SC, Sun Y, Yang TH, Chen YS, Yan BB, Li RD, Chen GY (2020) Biochar derived from corn stalk and polyethylene co-pyrolysis: characterization and Pb(II) removal potential. RSC Adv 10:6362–6376. https://doi.org/10.1039/c9ra09487c

Fang Z, Gao YR, Bolan N, Shaheen SM, Xu S, Wu XL, Xu XY, Hu HY, Lin JH, Zhang FB, Li JH, Rinklebe J, Wang HL (2020) Conversion of biological solid waste to graphene-containing biochar for water remediation: a critical review. Chem Eng J 390:124611. https://doi.org/10.1016/j.cej.2020.124611

Gao BQ, Li P, Yang R, Li AM, Yang H (2019a) Investigation of multiple adsorption mechanisms for efficient removal of ofloxacin from water using lignin-based adsorbents. Sci Rep 9:637. https://doi.org/10.1038/s41598-018-37206-1

Gao LY, Deng JH, Huang GF, Li K, Cai KZ, Liu Y, Huang F (2019b) Relative distribution of Cd^{2+} adsorption mechanisms on biochars derived from rice straw and sewage sludge. Bioresour Technol 272:114–122. https://doi.org/10.1016/j.biortech.2018.09.138

Gautam PK, Gautam RK, Banerjee S, Chattopadhyaya MC, Pandey JD (2016) Heavy metals in the environment: fate, transport, toxicity and remediation technologies. In: Pathania D (ed). Heavy metals: sources, toxicity and remediation techniques, Nova Sci Publishers 60:101–130.

Gundogdu A, Duran C, Senturk HB, Soylak M, Ozdes D, Serencam H, Imamoglu M (2012) Adsorption of phenol from aqueous solution on a low-cost activated carbon produced from tea industry waste: equilibrium, kinetic, and thermodynamic study. J Chem Eng Data 57:2733–2743. https://doi.org/10.1021/je300597u

Guo DL, Wu SB, Liu B, Yin XL, Yang Q (2012) Catalytic effects of NaOH and Na_2CO_3 additives on alkali lignin pyrolysis and gasification. Appl Energy 95:22–30. https://doi.org/10.1016/j.apenergy.2012.01.042

Han L, Qian LB, Liu RQ, Chen MF, Yan JC, Hu QH (2017) Lead adsorption by biochar under the elevated competition of cadmium and aluminum. Sci Rep 7:2264. https://doi.org/10.1038/s41598-017-02353-4

Huang XR, Zhao HH, Hu XF, Liu FH, Wang L, Zhao X, Gao PC, Ji PH (2020a) Optimization of preparation technology for modified coal fly ash and its adsorption properties for Cd^{2+}. J Hazard Mater 392:122461. https://doi.org/10.1016/j.jhazmat.2020.122461

Huang XR, Zhao HH, Zhang GB, Li JT, Yang Y, Ji PH (2020b) Potential of removing Cd(II) and Pb(II) from contaminated water using a newly modified fly ash. Chemosphere 242:125148. https://doi.org/10.1016/j.chemosphere.2019.125148

Kołodyńska D, Wnętrzak R, Leahy JJ, Hayes MHB, Kwapiński W, Hubicki Z (2012) Kinetic and adsorptive characterization of biochar in metal ions removal. Chem Eng J 197:295–305. https://doi.org/10.1016/j.cej.2012.05.025

Kołodyńska D, Gęca M, Pylypchuk IV, Hubicki Z (2016) Development of new effective sorbents based on Nanomagnetite. Nanoscale Res Lett 11:152. https://doi.org/10.1186/s11671-016-1371-3

Kong XK, Han ZT, Zhang W, Song L, Li H (2016) Synthesis of zeolite-supported microscale zero-valent iron for the removal of Cr^{6+} and Cd^{2+} from aqueous solution. J Environ Manag 169:84–90. https://doi.org/10.1016/j.jenvman.2015.12.022

Li H, McDonald AG (2014) Fractionation and characterization of industrial lignins. Ind Crop Prod 62:67–76. https://doi.org/10.1016/j.indcrop.2014.08.013

Liu Y, Fu RQ, Lou ZM, Fang WZ, Wang ZX, Xu XH (2015) Preparation of functional carbon-based materials for removal of heavy metals from aqueous solution. Prog Chem 27:1665–1678. https://doi.org/10.7536/PC150401

Liu TQ, Lawluvy Y, Shi Y, Ighalo JO, He Y, Zhang YJ, Yap P (2022) Adsorption of cadmium and lead from aqueous solution using modified biochar: a review. J Environ Chem Eng 10:106502. https://doi.org/10.1016/j.jece.2021.106502

Lu L, Yu WT, Wang YF, Zhang K, Zhu XM, Zhang YC, Wu YJ, Ullah H, Xiao X, Chen BL (2020) Application of biochar-based materials in environmental remediation: from multi-level structures to specific devices. Biochar 2:1–31. https://doi.org/10.1007/s42773-020-00041-7

Mahdi Z, El Hanandeh A, Yu QJ (2019) Preparation, characterization and application of surface modified biochar from date seed for improved lead, copper, and nickel removal from aqueous solutions. J Environ Chem Eng 7:103379. https://doi.org/10.1016/j.jece.2019.103379

Masindi V, Muedi KL (2018) Environmental contamination by heavy metals. In: Saleh HM, Aglan RFES (eds) Heavy metals, IntechOpen 10:115–132. https://doi.org/10.5772/intechopen.76082

Mason LH, Harp JP, Han DY (2014) Pb neurotoxicity: neuropsychological effects of lead toxicity. BioMed Res Int 2014:840547. https://doi.org/10.1155/2014/840547

Nan Q, Xin LQ, Qin Y, Waqas M, Wu WX (2021) Exploring long-term effects of biochar on mitigating methane emissions from paddy soil: a review. Biochar 3:125–134. https://doi.org/10.1007/s42773-021-00096-0

Nguyen TH, Pham TH, Nguyen Thi HT, Nguyen TN, Nguyen M-V, Tran Dinh T, Nguyen MP, Do TQ, Phuong T, Hoang TT, Mai Hung TT, Thi VHT (2019) Synthesis of iron-modified biochar derived from rice straw and its application to arsenic removal. J Chem 2019:5295610. https://doi.org/10.1155/2019/5295610

Pang HW, Huang SY, Wu YH, Yang DX, Wang XX, Yu SJ, Chen ZS, Alsaedi A, Hayat T, Wang XK (2018) Efficient elimination of U(VI) by polyethyleneimine-decorated fly ash. Inorg Chem Front 5:2399–2407. https://doi.org/10.1039/C8QI00253C

Qian LB, Chen BL (2013) Dual role of biochars as adsorbents for aluminum: the effects of oxygen-containing organic components and the scattering of silicate particles. Environ Sci Technol 47:8759–8768. https://doi.org/10.1021/es401756h

Qiu RF, Cheng FQ, Huang HM (2018) Removal of Cd^{2+} from aqueous solution using hydrothermally modified circulating fluidized bed fly ash resulting from coal gangue power plant. J Clean Prod 172:1918–1927. https://doi.org/10.1016/j.jclepro.2017.11.236

Rangabhashiyam S, Lins PVDS, Oliveira LMTM, Sepulveda P, Ighalo JO, Rajapaksha AU, Meili L (2022) Sewage sludge-derived biochar for the adsorptive removal of wastewater pollutants: a critical review. Environ Pollut 293:118581. https://doi.org/10.1016/j.envpol.2021.118581

Sajjadi B, Chen WY, Egiebor NO (2019) A comprehensive review on physical activation of biochar for energy and environmental applications. Rev Chem Eng 35:735–776. https://doi.org/10.1515/revce-2017-0113

Sarode S, Upadhyay P, Khosa MA, Mak T, Shakir A, Song S, Ullah A (2019) Overview of wastewater treatment methods with special focus on biopolymer chitin-chitosan. Int J Biol Macromol 121:1086–1100. https://doi.org/10.1016/j.ijbiomac.2018.10.089

Shen Y, Guo JZ, Bai LQ, Chen XQ, Li B (2021) High effective adsorption of Pb(II) from solution by biochar derived from torrefaction of ammonium persulphate pretreated bamboo. Bioresour Technol 323:124616. https://doi.org/10.1016/j.biortech.2020.124616

Sing KSW (1985) Reporting physisorption data for gas/solid systems with special reference to the determination of surface area and porosity (Recommendations 1984). Pure Appl Chem 57:603–619. https://doi.org/10.1351/pac198557040603

Teng DY, Zhang BB, Xu GM, Wang B, Mao K, Wang JX, Sun J, Feng XB, Yang ZG, Zhang H (2020) Efficient removal of Cd(II) from aqueous solution by pinecone biochar: sorption performance and governing mechanisms. Environ Pollut 265:115001. https://doi.org/10.1016/j.envpol.2020.115001

Tomczyk A, Sokołowska Z, Boguta P (2020) Biochar physicochemical properties: pyrolysis temperature and feedstock kind effects. Rev Environ Sci Biotechnol 19:191–215. https://doi.org/10.1007/s11157-020-09523-3

Trakal L, Bingöl D, Pohořelý M, Hruška M, Komárek M (2014) Geochemical and spectroscopic investigations of Cd and Pb sorption mechanisms on contrasting biochars: engineering implications. Bioresour Technol 171:442–451. https://doi.org/10.1016/j.biortech.2014.08.108

Wadhawan S, Jain A, Nayyar J, Mehta SK (2020) Role of nanomaterials as adsorbents in heavy metal ion removal from waste water: a review. J Water Process Eng 33:101038. https://doi.org/10.1016/j.jwpe.2019.101038

Wang H, Gao B, Wang S, Fang J, Xue Y, Yang K (2015a) Removal of Pb(II), Cu(II), and Cd(II) from aqueous solutions by biochar derived from $KMnO_4$ treated hickory wood. Bioresour Technol 197:356–362. https://doi.org/10.1016/j.biortech.2015.08.132

Wang SS, Gao B, Zimmerman AR, Li YC, Ma L, Harris WG, Migliaccio KW (2015b) Physicochemical and sorptive properties of biochars derived from woody and herbaceous biomass. Chemosphere 134:257–262. https://doi.org/10.1016/j.chemosphere.2015.04.062

Wang SS, Gao B, Li YC, Mosa A, Zimmerman AR, Ma LQ, Harris WG, Migliaccio KW (2015c) Manganese oxide-modified biochars: preparation, characterization, and sorption of arsenate and lead. Bioresour Technol 181:13–17. https://doi.org/10.1016/j.biortech.2015.01.044

Wang KF, Peng N, Sun JT, Lu GN, Chen MQ, Deng FC, Dou RN, Nie LJ, Zhong YM (2020) Synthesis of silica-composited biochars from alkali-fused fly ash and agricultural wastes for enhanced adsorption of methylene blue. Sci Total Environ 729:139055. https://doi.org/10.1016/j.scitotenv.2020.139055

Wu FF, Chen L, Hu P, Wang YX, Deng J, Mi BB (2021) Industrial alkali lignin-derived biochar as highly efficient and low-cost adsorption material for Pb(II) from aquatic environment. Bioresour Technol 322:124539. https://doi.org/10.1016/j.biortech.2020.124539

Xiao X, Chen BL, Chen ZM, Zhu LZ, Schnoor JL (2018) Insight into multiple and multilevel structures of biochars and their potential environmental applications: a critical review. Environ Sci Technol 52:5027–5047. https://doi.org/10.1021/acs.est.7b06487

Xiong XN, Yu IKM, Cao LC, Tsang DCW, Zhang SC, Ok YS (2017) A review of biochar-based catalysts for chemical synthesis, biofuel production, and pollution control. Bioresour Technol 246:254–270. https://doi.org/10.1016/j.biortech.2017.06.163

Xu YG, Bai TX, Yan YB, Ma KR (2020) Influence of sodium hydroxide addition on characteristics and environmental risk of heavy metals in biochars derived from swine manure. Waste Manag 105:511–519. https://doi.org/10.1016/j.wasman.2020.02.035

Yang Z, Xiong S, Wang B, Li Q, Yang W (2013) Cr(III) adsorption by sugarcane pulp residue and biochar. J Cent South Univ 20:1319–1325. https://doi.org/10.1007/s11771-013-1618-4

Yang Y, Wei ZB, Zhang XL, Chen X, Yue DM, Yin Q, Xiao L, Yang LY (2014) Biochar from *Alternanthera philoxeroides* could remove Pb(II) efficiently. Bioresour Technol 171:227–232. https://doi.org/10.1016/j.biortech.2014.08.015

Yang K, Jiang Y, Yang JJ, Lin DH (2018) Correlations and adsorption mechanisms of aromatic compounds on biochars produced from various biomass at 700 °C. Environ Pollut 233:64–70. https://doi.org/10.1016/j.envpol.2017.10.035

Yang X, Wan Y, Zheng Y, He F, Yu Z, Huang J, Wang H, Ok YS, Jiang Y, Gao B (2019) Surface functional groups of carbon-based adsorbents and their roles in the removal of heavy metals from aqueous solutions: a critical review. Chem Eng J 366:608–621. https://doi.org/10.1016/j.cej.2019.02.119

Yuan JH, Xu RK, Zhang H (2011) The forms of alkalis in the biochar produced from crop residues at different temperatures. Bioresour Technol 102:3488–3497. https://doi.org/10.1016/j.biortech.2010.11.018

Zama EF, Zhu Y, Reid BJ, Sun G (2017) The role of biochar properties in influencing the sorption and desorption of Pb(II), Cd(II) and As(III) in aqueous solution. J Clean Prod 148:127–136. https://doi.org/10.1016/j.jclepro.2017.01.125

Zama EF, Reid BJ, Sun GX, Yuan HY, Li XM, Zhu YG (2018) Silicon (Si) biochar for the mitigation of arsenic (As) bioaccumulation in spinach (*Spinacia oleracean*) and improvement in the plant growth. J Clean Prod 189:386–395. https://doi.org/10.1016/j.jclepro.2018.04.056

Zhang S, Ding J, Razanajatovo RM, Jiang H, Zou H, Zhu W (2019) Interactive effects of polystyrene microplastics and Roxithromycin on bioaccumulation and biochemical status in the freshwater fish red tilapia (*Oreochromis niloticus*). Sci Total Environ 648:1431–1439. https://doi.org/10.1016/j.scitotenv.2018.08.266

Zhang CT, Zhang ZM, Zhang LJ, Li QY, Li CC, Chen GZ, Zhang S, Liu Q, Hu X (2020) Evolution of the functionalities and structures of biochar in pyrolysis of poplar in a wide temperature range. Bioresour Technol 304:123002. https://doi.org/10.1016/j.biortech.2020.123002

Zhao ZD, Nie TT, Zhou WJ (2019) Enhanced biochar stabilities and adsorption properties for tetracycline by synthesizing silica-composited biochar. Environ Pollut 254:113015. https://doi.org/10.1016/j.envpol.2019.113015

Zhao HH, Huang XR, Liu FH, Hu XF, Zhao X, Wang L, Gao PC, Ji PH (2020a) A two-year field study of using a new material for remediation of cadmium contaminated paddy soil. Environ Pollut 263:114614. https://doi.org/10.1016/j.envpol.2020.114614

Zhao HH, Huang XR, Zhang GB, Li JT, He ZL, Ji PH, Zhao JZ (2020b) Possibility of removing cadmium pollution from the environment using a newly synthesized material coal fly ash. Environ Sci Pollut Res Int 27:4997–5008. https://doi.org/10.1007/s11356-019-07163-x

Zheng H, Wang ZY, Deng X, Zhao J, Luo Y, Novak J, Herbert S, Xing BS (2013) Characteristics and nutrient values of biochars produced from giant reed at different temperatures. Bioresour Technol 130:463–471. https://doi.org/10.1016/j.biortech.2012.12.044